2015

High-frequency normal-mode statistics in shallow water: The combined effect of random surface and internal waves

Raghukumara, Kaustubha; Colosi, John A.

Acoustical Society of America

Raghukumar, Kaustubha, and John A. Colosi. "High-frequency normal-mode statistics in shallow water: The combined effect of random surface and internal waves." The Journal of the Acoustical Society of America 137.5 (2015): 2950-2961.
https://hdl.handle.net/10945/71362

High-frequency normal-mode statistics in shallow water: The combined effect of random surface and internal waves

Kaustubha Raghukumar[a] and John A. Colosi
Oceanography Department, Naval Postgraduate School, Monterey, California 93943, USA

(Received 16 April 2014; revised 4 October 2014; accepted 25 March 2015)

In an earlier article, the statistical properties of mode propagation were studied at a frequency of 1 kHz in a shallow water environment with random sound-speed perturbations from linear internal waves, using a hybrid transport theory and Monte Carlo numerical simulations. Here, the analysis is extended to include the effects of random linear surface waves, in isolation and in combination with internal waves. Mode coupling rates for both surface and internal waves are found to be significant, but strongly dependent on mode number. Mode phase randomization by surface waves is found to be dominated by coupling effects, and therefore a full transport theory treatment of the range evolution of the cross mode coherence matrix is needed. The second-moment of mode amplitudes is calculated using transport theory, thereby providing the mean intensity while the fourth-moment is calculated using Monte Carlo simulations, which provides the scintillation index. The transport theory results for second-moment statistics are shown to closely reproduce Monte Carlo simulations. Both surface waves and internal waves strongly influence the acoustic field fluctuations. © *2015 Acoustical Society of America*. [http://dx.doi.org/10.1121/1.4919358]

[TFD] Pages: 2950–2961

I. INTRODUCTION

Acoustic scattering by various oceanographic phenomena leads to the statistical nature of sound propagation in both shallow and deep water environments. In a prior paper (Raghukumar and Colosi, 2014), we presented a statistical analysis of high frequency, shallow-water acoustic propagation in the presence of random linear internal wave-induced sound speed perturbations. In an environment similar to summer conditions in the mid-Atlantic bight as measured during the Shallow Water Experiment 2006 (SW06), mode coupling rates were found to be significant for lower order modes while mode coherences were adequately modeled by transport theoretic expressions derived using the adiabatic approximation that ignores mode coupling. Consequently, the cross-mode coherence matrix was efficiently modeled using a hybrid transport theory where the diagonal of the matrix (mode intensities) was calculated using a coupled-mode approach (Dozier, 1982; Creamer, 1996), while the off-diagonal terms (mode coherences) were modeled using adiabatic theory. New analytically tractable expressions were proposed to calculate the scattering matrix for internal waves modeled by the Garrett-Munk (GM) spectrum, and an efficient treatment of the "edge" effect was proposed (Colosi *et al.*, 2012b), wherein an over-counting of range terms from behind the source was corrected in the scattering matrix computation. In this companion paper, we extend our transport theory analysis for internal waves to include the effect of random surface waves, as derived by Thorsos *et al.* (2010).

While random linear internal waves are a dominant cause of acoustic scattering at low frequencies, at higher frequencies, particularly in shallow water, the presence of surface- and bottom-interacting modes leads to additional scattering by surface waves and an undulating seabed. Early experimental work by Brown (1969) established the relation between intensity fluctuations and surface roughness. More recently, Dahl (1999) compared experimental measurements of mean intensity with a model for bistatic sea surface scattering in shallow water at a frequency of 30 kHz. While much theoretical work on surface scattering has focused on modeling scattering strength and reverberation effects by rough surface scattering (Eckart, 1953; Thorsos, 1990; McDaniel, 1993), there have also been some efforts to understand mode coupling by surface waves (Beilis and Tappert, 1979; Rouseff and Ewart, 1995) and its effect on long range propagation. However, to the extent of our knowledge, no effort has been made to examine the combined effect of both internal and surface waves on the statistical moments of the acoustic field at long ranges.

Transport theory is an approach that provides the range evolution of various moments of a stochastic acoustic field. Scattering theory for mode coupling and phase randomization phenomena by random linear internal waves appears to have gained solid theoretical ground in a series of recent papers applied to deep and shallow water environments, from 200 Hz to 1 kHz (Creamer, 1996; Colosi and Morozov, 2009; Colosi *et al.*, 2012b; Raghukumar and Colosi, 2014). A transport theory framework for mode coupling by surface waves has also recently been demonstrated in shallow water at 3 kHz by Thorsos *et al.* (2004) and Thorsos *et al.* (2010), where second- and fourth-moment statistics of mode amplitudes were compared against Monte Carlo simulations, with a rough sea-surface modeled using a one-dimensional Pierson-Moskowitz (PM) spectrum.

[a]Electronic mail: kraghuku@nps.edu

 0001-4966/2015/137(5)/2950/12/$30.00

Here, we combine the transport theory approach as presented by Raghukumar and Colosi (2014) with Thorsos' treatment to look at the combined effects of shallow water internal and surface waves on mode coupling at high frequencies (1 kHz). Previously derived analytical expressions for the internal-wave scattering matrix are modified to include the effect of surface waves as modeled by the PM spectrum (Pierson and Moskowitz, 1964). Unlike the case of internal wave scattering, which preferentially couples lower-order modes, we find that mode coupling by surface waves primarily couples higher-order surface-interacting modes. The importance of these higher modes depends on the relative rates of attenuation and mode coupling. The combined effect of both internal and surface waves is a superposition of the effects of each individual phenomenon, with mode coupling and phase randomization occurring over all modes. Additionally, surface wave-induced mode coherences are found to be strongly influenced by mode coupling, with the previously proposed internal wave hybrid transport theory utilizing the adiabatic approximation no longer sufficient to model the cross-mode coherence matrix. The importance of surface wave-induced acoustic mode coupling is demonstrated in the Monte Carlo calculations of the mode amplitude fourth-moment, where the scintillation index (SI) calculated using the adiabatic approximation is shown to be vastly different than the full-field calculation that takes into account mode coupling effects.

The organization of this paper is as follows. In Sec. II, we provide an overview of transport theory, and present expressions for mode coherences based on new expressions for the scattering matrix in the presence of surface waves. Also described are the new transport theory calculations, necessary for handling surface waves. Section III describes the modeled SW06 environment, along with computational methods employed in the Monte Carlo simulations with surface and internal waves. Section IV contains results comparing the separate and joint effects of surface and internal waves on acoustic mode coupling and phase randomization. Finally, Sec. V concludes the paper and analyzes mode coupling and coherence effects in a high frequency regime in shallow water with rough sea surface and volume scattering.

II. TRANSPORT THEORY

We begin with well-documented background material on transport equations for the range evolution of the cross-mode coherence matrix (Colosi and Morozov, 2009). This background material is necessary to make this manuscript relatively self-contained. Both surface- and internal-wave effects are considered, and we draw heavily from the transport theory results of Thorsos *et al.* (2010) and Raghukumar and Colosi (2014).

Using a two-dimensional (2D) normal mode-based approach, the acoustic pressure field, $p(r,z)$ can be expressed as

$$p(r,z)=\sum_{n=1}^{N}\frac{a_n(r)\phi_n(z)}{\sqrt{k_n r}}, \tag{1}$$

where, following the perturbational approach of Jensen *et al.* (1994), $\phi_n(z)$ is the unperturbed real mode shape, calculated by neglecting any attenuation effects, and $l_n=k_n+i\alpha_n$ is the complex eigen-wavenumber where α_n is computed from perturbation theory. All variability is contained in the range-dependent mode amplitude, $a_n(r)$.

Dozier (1982) and Creamer (1996) expressed the evolution of mode amplitudes in shallow water as

$$\frac{da_n}{dr}-il_n a_n=-i\sum_{m=1}^{N}\Gamma_{mn}(r)a_m(r), \tag{2}$$

where $\Gamma_{mn}(r)$ is the symmetric coupling matrix which in our case accounts for internal and surface waves. If the energy transfer between internal and surface waves is small [between 10^{-6} and 10^{-4} W/m^2 according to Olbers and Herterich (1979) and Watson (1994)], one can safely assume that internal and surface wave effects on acoustic mode coupling are separable. The combined symmetric mode coupling matrix can then be simply written as $\Gamma_{mn}(r)=\Gamma^{IW}_{mn}(r)+\Gamma^{SW}_{mn}(r)$. In the presence of small surface wave-induced sea surface height perturbations, and ignoring important 2D surface scattering effects, the mode coupling matrix $\Gamma^{SW}_{mn}(r)$ is given by [Thorsos *et al.* (2010), complete derivation pending publication]

$$\Gamma^{SW}_{mn}(r)=-\frac{h(r)}{2\rho_0(0)}\frac{1}{\sqrt{k_n k_m}}\frac{d\phi_n}{dz}\frac{d\phi_m}{dz}, \tag{3}$$

where $h(r)$ is the surface displacement, and the depth-derivatives are evaluated at the surface, $z=0$. In comparison, the symmetric mode coupling matrix with internal wave-induced sound-speed perturbations is given by (Dozier and Tappert, 1978a; Colosi and Morozov, 2009)

$$\Gamma^{IW}_{mn}(r)=\frac{k_0^2}{\sqrt{k_n k_m}}\int_0^D\frac{\phi_n(z)\phi_m(z)}{\rho_0(z)}\frac{\delta c(r,z)}{c_0}dz, \tag{4}$$

where $\delta c(r,z)$ is the sound-speed perturbation, c_0 is a representative sound speed, D is the water depth, $\rho_0(z)$ is the density profile, and $k_0=\omega/c_0$ is a representative wavenumber.

Transport theory provides expressions for the range evolution of various moments of intensity such as the first moment, $\langle I\rangle=\langle|p|^2\rangle$, and second-moment $\langle I^2\rangle=\langle|p|^4\rangle$. The mean intensity is given by

$$\langle I(r,z)\rangle=\langle|p(r,z)|^2\rangle=\sum_{n=1}^{N}\sum_{p=1}^{N}\frac{\langle a_n a_p^*\rangle(r)}{r}\frac{\phi_n(z)\phi_p(z)}{\sqrt{k_n k_p}}, \tag{5}$$

where $\langle a_n a_p^*\rangle(r)$ can be recognized as the cross-mode coherence matrix.

Using transport theory (Creamer, 1996; Colosi and Morozov, 2009) the range evolution of the cross-mode coherence matrix can be expressed as

$$\begin{aligned}\frac{d\langle a_n a_p^*\rangle}{dr}&+i\left(l_p^*-l_n\right)\langle a_n a_p^*\rangle\\&=\sum_{m=1}^{N}\sum_{q=1}^{N}\langle a_m a_q^*\rangle I^*_{mn,qp}+\langle a_q a_m^*\rangle I_{mp,qn}\\&\quad-\langle a_n a_q^*\rangle I^*_{mp,qm}-\langle a_q a_p^*\rangle I_{mn,qm},\end{aligned} \tag{6}$$

where $I_{mn,qp}$, known as the scattering matrix is given by

$$I_{mn,qp} = \int_0^\infty d\xi \Delta_{mn,qp}(\xi) e^{-ik_{qp}\xi}. \tag{7}$$

Here $\Delta_{mn,qp}(\xi) = \langle \Gamma_{mn}(r)\Gamma_{qp}(r+\xi)\rangle$ is the correlation function of the symmetric mode coupling matrix [Eq. (4)], for range separation ξ. The acoustic mode wavenumber difference is $k_{qp} = k_p - k_q$. Given that internal and surface waves are uncorrelated phenomena, $\Delta_{mn,qp}(\xi)$ can be expressed as a sum of the correlations of symmetric mode coupling matrices for internal and surface waves,

$$\Delta_{mn,qp}(\xi) = \langle \Gamma^{SW}_{mn}(r)\Gamma^{SW}_{qp}(r+\xi)\rangle + \langle \Gamma^{IW}_{mn}(r)\Gamma^{IW}_{qp}(r+\xi)\rangle. \tag{8}$$

Thus, the scattering matrix, Eq. (7), can be composed by contributions from both surface and internal waves.

A. Internal wave scattering matrix

The correlation operation needed to calculate $\Delta_{mn,qp}(\xi)$ can be recast as an inverse Fourier transform of an isotropic wavenumber spectrum of either sound speed-, or sea surface height-perturbations. This operation allowed Colosi *et al.* (2012b) to write the scattering matrix for internal waves as

$$I_{mn,qp} = \sum_{j=1}^{J} G_{mn}(j)G_{qp}(j) \int_0^\infty dk\, S_j(k) \times \begin{cases} \dfrac{1}{\sqrt{k^2 - k_{pq}^2}}, & 0 \le |k_{pq}| < k, \\ \dfrac{i\,\mathrm{sgn}\,(k_{pq})}{\sqrt{k_{pq}^2 - k^2}}, & 0 \le k < |k_{pq}|. \end{cases} \tag{9}$$

Here, J is the maximum internal wave mode number and $G_{mn}(j)$ is given by

$$G_{mn}(j) = k_0^2 \sqrt{\frac{2}{k_n k_m}} \int_0^D dz \langle \mu^2(z)\rangle^{1/2} \times \sin[\pi j \hat{z}(z)] \frac{\phi_n(z)\phi_m(z)}{\rho_0(z)}, \tag{10}$$

with $\hat{z}(z)$ being the Wentzel-Kramers-Brillouin (WKB) stretched vertical coordinate. The fractional sound speed variance, $\langle \mu^2(z)\rangle$ is given by

$$\langle \mu^2(z)\rangle = \frac{\zeta_0^2}{c_0^2}\frac{N_0}{N(z)}\left(\frac{dc}{dz}\right)_p^2, \tag{11}$$

where ζ_0 is a reference displacement, N_0 is a reference buoyancy frequency, $N(z)$ is the Brünt-Vaisala buoyancy frequency, and $(dc/dz)_p$ is the potential sound-speed gradient. The validity of WKB scaling in shallow water was examined by Colosi *et al.* (2012a), who compared WKB mode functions to those derived from the linear internal wave mode equations. With the exception of mode 1 [see Fig. 2, Colosi *et al.* (2012a)], which is to be expected for WKB analysis, a good approximation to the dynamic modes was seen between the inertial frequency and ~2 cph. That being said, shallow water has a larger fraction of mode 1 energy than deep water.

While Colosi *et al.* (2012b) evaluated the wavenumber integral in Eq. (9) numerically, Raghukumar and Colosi (2014) derived new closed-form expressions when $S_j(k)$ is parametrized by a GM spectrum,

$$S_j(k) = H(j)\frac{4}{\pi}\frac{k^2 k_j}{\left(k^2 + k_j^2\right)^2}. \tag{12}$$

Here $k_j = \pi f j/N_0 B$, f is the Coriolis frequency, $N_0 B = \int_0^D N(z)dz$ is the internal wave energy parameter, and $H(j) = N_j/(j^2 + j_*^2)$ is the GM vertical mode spectrum with N_j being the normalization factor, and j_* the modal band width parameter. While the GM spectrum was originally proposed as a canonical deep-water internal wave spectrum (Garrett and Munk, 1979), a calculation of the diffuse internal wave frequency and mode spectrum from SW06 measurements by Colosi *et al.* (2012b) was found to be quite close to the GM model when $j_* = 1$.

The final form for the internal wave scattering matrix was given by

$$I_{mn,qp} = \sum_{j=1}^{J} G_{mn}(j)G_{qp}(j)H(j)\frac{4a}{\pi|k_{qp}|}\left[\frac{\cos\theta_{\min}}{(a^2+1)(a^2+2-a^2\cos 2\theta_{\min})} + \frac{\mathrm{atanh}\left(\sqrt{\frac{a^2}{a^2+1}}\cos\theta_{\min}\right)}{2a(a^2+1)^{3/2}} + i\frac{\pi\,\mathrm{sgn}\,(k_{pq})}{4a(a^2+1)^{3/2}}\right], \tag{13}$$

where $a = k_j/|k_{qp}|$, $\sin\theta_{\min} = |k_{qp}|f/(k_j N_{\max})$, with $N_{\max}$ the maximum buoyancy frequency.[1] For the special case of $k_{qp} = 0$, the terms following $H(j)$ in Eq. (13) simplify to $(2/\pi)(1/k_j)(k_{\max}^2/k_{\max}^2 + k_j^2)$ where $k_{\max}$ is a maximum wavenumber chosen to ignore the inaccurate high-wavenumber roll-off characteristics of the WKB internal wave dispersion relation (Colosi *et al.*, 2013).

B. Surface wave scattering matrix

Similar to Eq. (9) for internal waves, the scattering matrix for surface waves can be written as

$$I_{mn,qp} = \frac{1}{4\rho^2(0)} \frac{1}{\sqrt{k_m k_n k_p k_q}} \frac{d\phi_m}{dz}\frac{d\phi_n}{dz}\frac{d\phi_q}{dz}\frac{d\phi_p}{dz} \times \int_0^\infty dk\, S_h(k) \begin{cases} \dfrac{1}{\sqrt{k^2 - k_{pq}^2}}, & 0 \le |k_{pq}| < k, \\ \dfrac{i\,\mathrm{sgn}(k_{pq})}{\sqrt{k_{pq}^2 - k^2}}, & 0 \le k < |k_{pq}|, \end{cases} \tag{14}$$

where once again, the depth-derivatives are evaluated at $z = 0$, and $S_h(k)$ is an arbitrary isotropic horizontal wavenumber spectrum for surface waves. Similar to Thorsos *et al.* (2010), we use the isotropic PM spectrum for $S_h(k)$, given by

$$S_h(k) = \frac{\alpha}{2k^3}\exp\left[-\frac{k_L^2}{k^2}\right], \tag{15}$$

where $\alpha = 8.1 \times 10^{-3}$, $k_L^2 = \beta g^2/U^4$, $\beta = 0.74$, $g = 9.8\,\mathrm{m/s^2}$, and U is the wind speed in m/s. For this model $\langle h^2 \rangle = \alpha U^4/4\beta g^2$.

Substitution of Eq. (15) into Eq. (14) results in the following expression for the wavenumber integral:

$$\int_0^\infty \frac{S_h(k)}{\sqrt{k^2 - k_{qp}^2}}dk = \frac{\alpha}{2|k_{qp}|^3}\int_0^\infty e^{-a^2x^2}\frac{x^2}{\sqrt{1-x^2}}dx, \tag{16}$$

where $x = |k_{qp}|/k$ and $a^2 = k_L^2/k_{qp}^2$. While Eq. (16) can be solved numerically, greater numerical tractability can be obtained by making a trigonometric substitution that results in an integral given by

$$\int_0^\infty \frac{S_h(k)}{\sqrt{k^2 - k_{qp}^2}}dk = \frac{\alpha}{2|k_{qp}|^3}\left[\int_0^{\pi/2} e^{-a^2\sin^2\theta}\sin^2\theta\, d\theta + i\,\mathrm{sgn}\,(k_{pq})\int_0^{\pi/2} e^{-a^2/\sin^2\theta}\frac{d\theta}{\sin^3\theta}\right]. \tag{17}$$

The scattering matrix for surface waves can therefore be easily numerically evaluated by substitution of Eq. (17) into Eq. (14).

III. NUMERICAL COMPUTATIONS FOR THE SW06 ENVIRONMENT

This section describes the modeled acoustic propagation scenario, specifically pertaining to surface waves. The acoustical waveguide with internal waves is identical to that described in the companion paper, Raghukumar and Colosi (2014), and is only briefly described here. Also described here are the Monte Carlo simulations, and the numerical implementation of the surface wave transport equations for mode coherence.

The propagation environment is similar to that measured during the SW06 experiment, conducted off the New Jersey continental shelf. Further details of the experiment and the acoustic fluctuations observed may be found in the papers by Lynch and Tang (2008) and Colosi *et al.* (2012a). The acoustic frequency is chosen to be 1000 Hz, with a constant water depth of 86 m over a 50 km range. The source depth is 25 m for this study corresponding to the sound speed minimum. Bottom attenuation is fixed at $\alpha^\lambda = 0.2\ \mathrm{dB}/\lambda$, and water column attenuation is also included (Munk *et al.*, 1995). The density of the water column and sea bottom are fixed at 1000 and 1500 $\mathrm{kg/m^3}$, respectively. The reference sound speed in the water column is 1500 m/s, and bottom sound speed is 1700 m/s. All features of the acoustical waveguide such as density parameters, sub-bottom sound speed, sub-bottom and water column attenuation parameters are identical to that studied in Raghukumar and Colosi (2014). Thus, insights into the statistics of sound propagation in the presence of surface waves can be seamlessly compared to the previously studied acoustical statistics in the presence of random linear internal waves.

A. Environmental characteristics

The SW06 experiment was a multi-disciplinary, multi-institutional effort with particular emphasis on the acoustical effects of non-linear internal waves. The Mid-Atlantic Bight experimental layout was in a T-shaped pattern (Tang *et al.*, 2007), with a cluster of acoustic and oceanographic instrumentation at the center of the "T," that included surface wave measurements by a TRIAXYS directional wave buoy (AXYS Technologies Inc., British Columbia, Canada) and an Air-Sea Interaction Spar buoy deployed by the University of Miami. These systems recorded wind speeds of 6 m/s (±1 m/s) over a 6.5 h period on August 10, 2006 (Dahl, 2010), with a root-mean-square wave height of 0.16 m (±10%) over the measurement period. These wind speeds indicate a Beaufort sea state 4, with a moderate breeze and fairly frequent whitecaps, including small waves with breaking crests. While these sea surface conditions are not reflective of fully developed seas, we nevertheless use a non-directional PM spectrum to model surface waves, as was done by Thorsos *et al.* (2010) for the SW06 environment. In this paper we use a wind speed of 5.5 m/s for the majority of transport theory analysis, and occasionally include results at 10 m/s for illustrative purposes. A more complete analysis of surface wave conditions during the entire month of August of SW06, including directional aspects and a comparison to other canonical spectra such as the JONSWAP spectrum is beyond the scope of this paper, but will certainly be necessary when transport theory predictions are compared against acoustic data.

B. Monte Carlo simulations

Repeated realizations of both internal and surface waves are employed in this paper in order to compare transport theory results with Monte Carlo simulations.

Random linear internal wave-induced sound-speed fluctuations were simulated using the technique of Colosi and Brown (1998) for a shallow water version of the Garett-Munk (GM) spectrum. During the SW06 experiment,

packets of nonlinear internal waves were likely present on the acoustic transmission path. The GM spectrum does not model these nonlinear internal waves, which do not follow Gaussian statistics. Further, variability introduced by the internal tide is also absent in the GM model. That being said, Colosi *et al.* (2012a) found that nonlinear internal waves have little impact on the moments of the acoustic field when random linear internal waves are also present, due to the prior decorrelation and phase randomization by linear internal waves. Various parameters for the GM linear internal wave model include $\zeta_0 = 2$ m, $N_0 = 3$ cph, $j_* = 1$, and latitude 39°N. The maximum number of internal wave modes was 15, and internal wave horizontal scales ranged from 20 m to 100 km.

Realizations of sea surface height perturbations with Gaussian statistics that follow the PM spectrum are obtained using the spectral method of Thorsos (1988). In order to generate sea surface height realizations that obey the PM spectrum for Monte Carlo simulations, the isotropic form of the spectrum, Eq. (15), is written in the Cartesian k_x spectral form,

$$S_h(k_x) = \frac{\alpha}{2\pi}\frac{1}{|k_x|^3}\int_0^{\pi/2} \exp\left(-\frac{k_L^2\cos^2\theta}{k_x^2}\right) \times \cos^2\theta d\theta \quad \text{for } |k_x| > 0, \\ = \frac{\alpha}{8k_L^3\sqrt{\pi}} \quad \text{for } k_x = 0, \tag{18}$$

where the integral is numerically evaluated. The cutoff wavenumbers (k_L) for wind speeds of 5.5 and 10 m/s are 0.23 and 0.08 m^{-1}, respectively. For a wind speed of 5.5 m/s, the PM spectrum excites higher wavenumbers that occupy the roll-off region of the GM-spectrum. This has implications for the resonant conditions in transport theory where mode coupling between acoustic modes is greatest when the acoustic beat wavenumber is equal to the wavenumber of an inhomogeneity, either in the form of surface or internal waves. The broadening of the wavenumber spectrum from random processes therefore increases the potential for acoustic mode coupling by allowing for coupling across a broader range of acoustic beat wavenumbers.

For each sea surface and/or sound speed perturbation field, acoustic mode amplitudes are computed using Eq. (2), where the first-order differential equation is numerically solved using an eigenvector technique (Dozier and Tappert, 1978b), with a range step of 5 m. Mean mode energies, coherences, and intensities are then calculated over 256 realizations of surface and internal waves. A limitation of Eq. (3) for surface waves is the approximation that the range evolution of mode amplitudes is linear in h, the sea surface height perturbation. For the environment considered, this small perturbation approximation was found to be valid for wind speeds up to about 6 m/s above which unreasonably large mode coupling is predicted by the Monte Carlo simulations. However, transport theory calculations appeared relatively robust up to wind speeds of 10 m/s, with no unreasonable numerical artifacts observed. Thorsos *et al.* (2010) found good agreement with Monte Carlo simulations for a wind speed of 7.7 m/s. While a higher-order approximation has been recently proposed by Henyey and Thorsos (2013), a transport theoretic framework for the acoustic moments using this higher-order approximation is currently absent. Consequently, to preserve consistency with the transport theory analysis, Monte Carlo simulations are conducted using the linear in h approximation for the mode coupling matrix. This is clearly a first step forward.

Figure 1 shows an example of acoustic propagation of a 1000 Hz signal, over a range of 50 km, with a source located at a depth of 25 m. Shown are the unperturbed intensity and perturbed intensities for a single realization of the surface wave field, and surface and internal wave field in combination. The intensities are normalized by the maximum unperturbed intensity, and cylindrical spreading is omitted in the intensity calculation. The inset shows the intensities over a 5 km region between 30 and 35 km. The unperturbed intensity plot shows the effect of higher order mode stripping by interaction with the sea bottom, thus giving rise to an interference pattern dominated by lower order modes at longer ranges. This interference pattern is noticeably affected by the presence of surface and internal waves. Mode coupling by surface waves leads to increased insonification close to the surface, while mode coupling by internal waves leads to enhanced insonification close to the bottom.

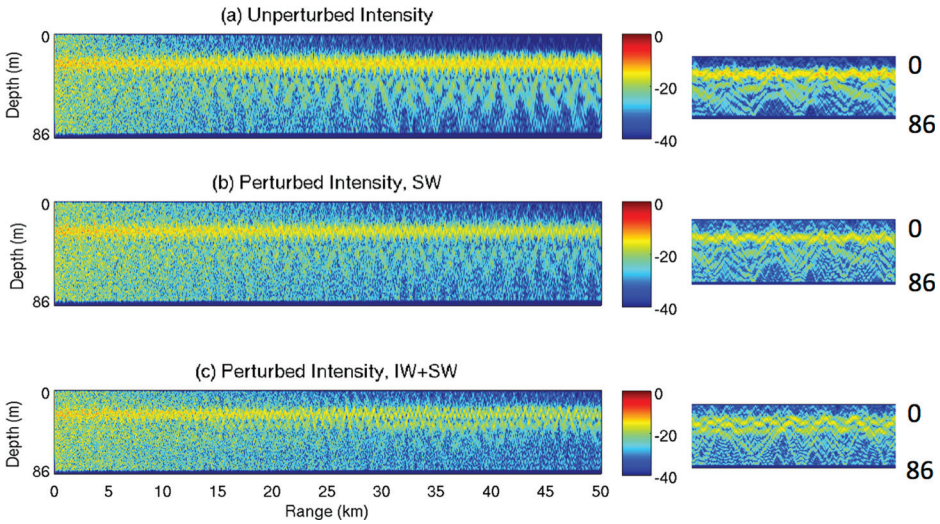

FIG. 1. An example showing the normalized acoustic intensity (dB re 1 μPa): (a) with no perturbations, (b) with a perturbed sea surface, and (c) with a perturbed sound speed field and a perturbed sea surface. The insets show the respective intensities between 30 km and 35 km.

C. Transport theory computations

Transport theory calculations for the range evolution of the mode coherence matrix are made by solving the full-coherence equation, Eq. (6), using a variable order Adams-Bashforth-Moulton method. The scattering matrix for internal waves is given by the analytical expression, Eq. (13), and the surface wave scattering matrix is calculated by numerically evaluating Eq. (14).

IV. RESULTS

Various aspects of transport theory are presented that provide insight into the mode-number dependence of mode coupling phenomena in the presence of surface waves. Since the transport theory computations were numerically robust up to wind speeds of 10 m/s (though unsubstantiated by Monte Carlo simulations at this higher wind speed), transport theory results in Secs. IV A and IV B are presented at wind speeds of 5.5 and 10 m/s, primarily to illustrate the effect of a higher sea state on various mode coupling metrics.

Monte Carlo simulations of acoustic propagation through perturbed fields are then employed to validate transport theory observables such as mode energies, cross-mode coherences and mean intensity at 1000 Hz, for a wind speed of 5.5 m/s. Finally, the effect of surface and internal waves on the SI is demonstrated using Monte Carlo simulations.

A. Mode coupling range versus attenuation range

The relative rates (in range) of mode coupling and attenuation are studied in this section in order to understand which modes have an opportunity to interact and randomize the phases of other modes before attenuation effectively removes these modes from the water column. The competing effects of coupling and attenuation are demonstrated for surface waves in the absence and presence of internal waves.

In the absence of attenuation, the mode energy equation (Dozier and Tappert, 1978a), can be written as

$$\frac{d\mathbf{a}}{dr} = \mathbf{F}\mathbf{a}, \tag{19}$$

where $\mathbf{a}$ is a vector of mode energies, and $\mathbf{F}$ is derived from the scattering matrix, with the individual elements of $\mathbf{F}$ given by

$$F_{mn} = 2\mathrm{Re}(I_{mn,mn}) \quad \text{for } m \neq n,$$
$$F_{nn} = -\sum_{m=1,m\neq n}^{N} 2\mathrm{Re}(I_{mn,mn}). \tag{20}$$

The solution to Eq. (19) can be written in terms of the eigenvalues and eigenvectors of $\mathbf{F}$. The eigenvalues of $\mathbf{F}$ represent the exponential decay rate of the corresponding eigenvectors, and the inverse of the second eigenvalue gives the equipartition range (Dozier and Tappert, 1978a). If each eigenvector is dominated by a single mode, as they were found to be for the current propagation scenario, then the index of the dominating mode in the eigenvector approximately identifies the eigenvalue that now represents energy decay rate for the dominating mode. The inverse of the eigenvalues, $R_n = 1/\lambda_n$, therefore represents the e-folding range over which the relevant mode is coupled, and is defined as the mode coupling range. Similarly, the mode attenuation range, defined as $P_n = [2\alpha_n]^{-1}$, is the e-folding range over which a mode undergoes sub-bottom and water column attenuation. In the presence of internal waves alone, low modes with turning point depths in the thermocline region have a shorter mode coupling range than the attenuation range, allowing for mode coupling to take precedence over mode attenuation (Raghukumar and Colosi, 2014). Conversely, higher modes, with turning point depths outside the thermocline can be stripped out of the water column by attenuation well before the occurrence of mode coupling.

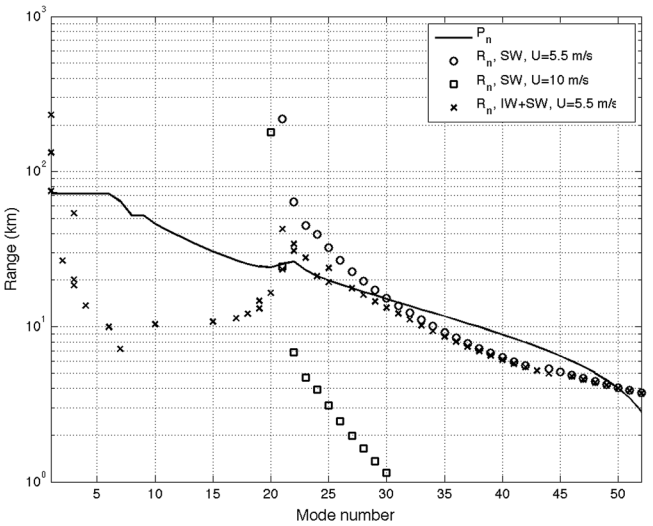

FIG. 2. Mode coupling (R_n) and attenuation (P_n, solid line) ranges in kilometers, in the presence of surface waves alone (circle, square) or internal and surface waves (cross), at 1000 Hz for wind speeds of 5.5 and 10 m/s. Note that the attenuation is constant for low modes that are only subject to water column attenuation and no bottom interaction/attenuation.

Figure 2 shows the attenuation range (solid line) overlaid with the mode coupling range at 1000 Hz for three fluctuation scenarios: (1) surface waves, with a wind speed of 5.5 m/s (circles), (2) surface waves, with a wind speed of 10 m/s (squares), and (3) internal and surface waves, with a wind speed of 5.5 m/s (crosses). At the lower wind speed, only modes above mode 30 have a shorter coupling range than the attenuation range, and can undergo coupling before being attenuated. Further, modes above mode 35 have attenuation ranges less than 10 km, suggesting that mode coupling phenomena for these modes are only observed at short ranges, on the order of a few kilometers, after which they are stripped out of the water column. Increasing the wind speed to 10 m/s results in a significant lowering of the mode coupling range for modes above mode 22, allowing for the observation of mode coupling effects over longer distances. Finally, the combined effect of internal and surface waves is that mode coupling effects can now be observed over the entire mode spectrum, at a wide range of e-folding scales, that in general, decrease with mode number.

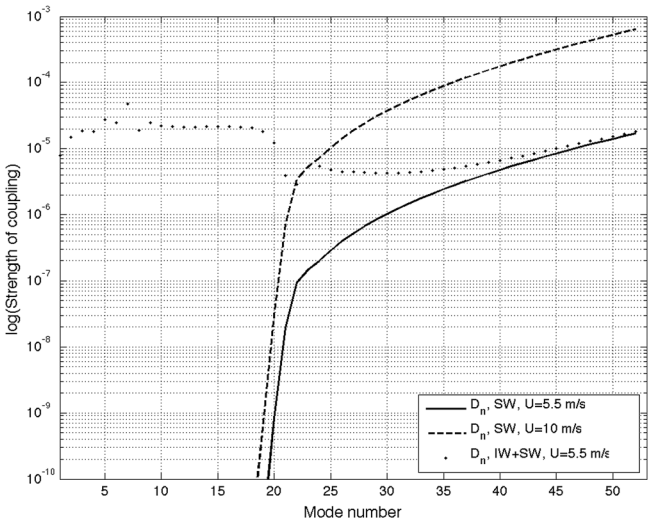

FIG. 3. Strength of nearest neighbor mode coupling (m^{-1}) at 1000 Hz in the presence of surface waves alone (solid line, dashed line), or internal and surface waves (dotted line), for wind speeds of 5.5 and 10 m/s.

B. Strength of mode coupling

The mode energy equation, Eq. (19), was further analyzed by Raghukumar and Colosi (2014), based on a proposed metric that measures the strength of mode coupling.

The assumption of small angle scattering leads to the strongest mode coupling by nearest-neighbor mode pairs, and the matrix **F** [Eq. (20)] was verified to be strongly peaked along the diagonal. The near neighbor elements of $2\,\mathrm{Re}(I_{mn,mn})$ represent a measure of energy transfer between neighboring modes. Raghukumar and Colosi (2014) proceeded to show that in the presence of internal waves, the strongest coupling occurs in low modes with turning point depths close to the thermocline, where internal wave activity is the strongest.

Figure 3 plots the mode coupling strength versus mode number for the three perturbation scenarios described in Sec. IV A. In the presence of surface waves (solid and dashed lines), modes greater than mode 22 have significantly stronger mode coupling than lower modes. It is pointed out that mode 22 represents a transition in mode turning depths, above which the upper turning depth is at the surface [see Raghukumar and Colosi (2014), Fig. 5]. The effect of increasing wind speed is an increase in the strength of coupling by approximately an order of magnitude. Finally, the introduction of internal waves (dotted lines) into the perturbation scenario results in low modes having a significant strength of mode coupling, in addition to high mode coupling by surface waves.

C. Mode energies

The preferential coupling of modal subsets by surface and internal waves can most easily be observed in the range evolution of mode energies. In addition, the validity of the surface and internal wave transport theory in predicting the evolution of mode energies is demonstrated by comparison to Monte Carlo simulations.

In order to focus on mode coupling effects, attenuation is ignored, and mode energies are calculated using Eq. (19). Figure 4 shows the range evolution over 50 km of mean mode energies for modes 1–3, 18–20, and 51–53, for the case with surface waves alone, for a wind speed of 5.5 m/s. Figure 5 shows mode energies when both surface and internal waves are present. In both Figs. 4 and 5, dashed lines show transport theory, and the solid lines show Monte Carlo simulations. All curves are seen to have a good agreement with Monte Carlo simulations.

As indicated by Fig. 3, surface waves preferentially couple high modes that have their upper turning depths at the

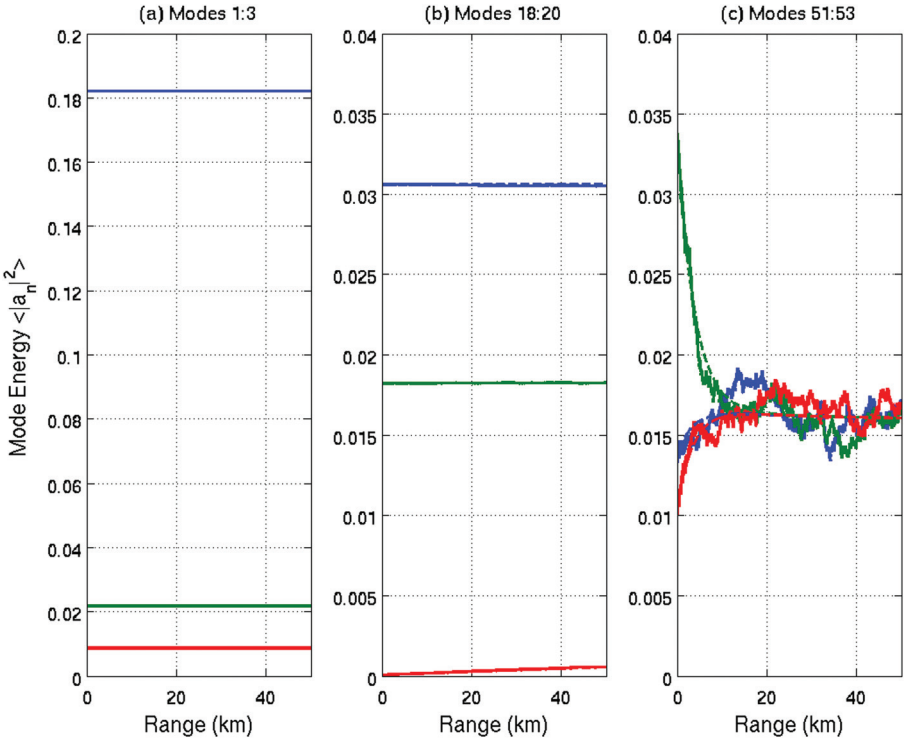

FIG. 4. Mode energies for the case with surface waves alone, scaled to remove attenuation effects in order to focus on coupling effects. Shown are mode energies for modes: (a) 1–3 (blue, green, and red, respectively), (b) 18–20 (blue, green, and red, respectively), and (c) 51–53 (blue, green, and red, respectively). Monte Carlo simulation is the solid line and transport theory is the dashed line.

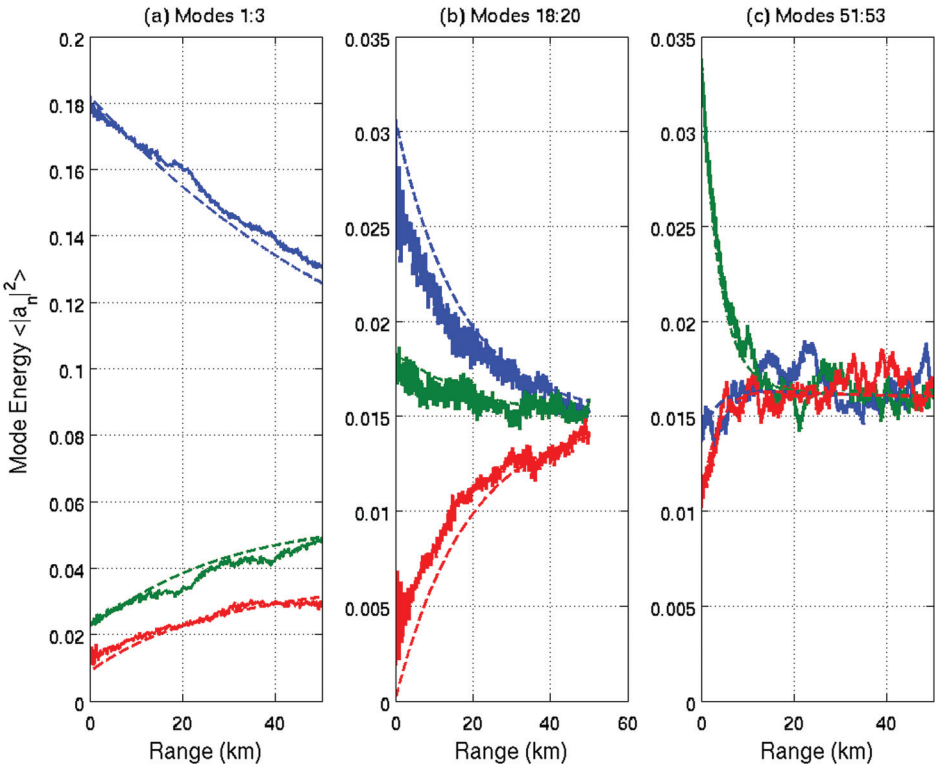

FIG. 5. Mode energies for the case with surface and internal waves, scaled to remove attenuation effects in order to focus on coupling effects. Shown are mode energies for modes: (a) 1–3 (blue, green, and red, respectively), (b) 18–20 (blue, green, and red, respectively), and (c) 51–53 (blue, green, and red, respectively). Monte Carlo simulation is the solid line and transport theory is the dashed line.

surface, while the lower modes propagate adiabatically, i.e., without any transfer of energy to higher or lower modes. The strong coupling of high modes results in a rapid drive towards equipartition within 5 km of propagation, a result roughly consistent with the predicted e-folding range for mode coupling in Fig. 2.

In the presence of both surface and internal waves (Fig. 5), mode coupling now occurs over the entire mode spectrum, with lower modes coupled in an identical manner to results presented in Raghukumar and Colosi (2014), while higher modes remain exclusively coupled by surface waves. The increasing decay rate across the mode spectrum was studied by Dozier and Tappert (1978a), and found to be the consequence of increasing magnitude of eigenvectors of the symmetric scattering matrix, $2\,\mathrm{Re}(I_{mn,mn})$, whose eigenvalues are ordered such that $\lambda_1 = 0 \geq \lambda_2 \geq \cdots \geq \lambda_N$.

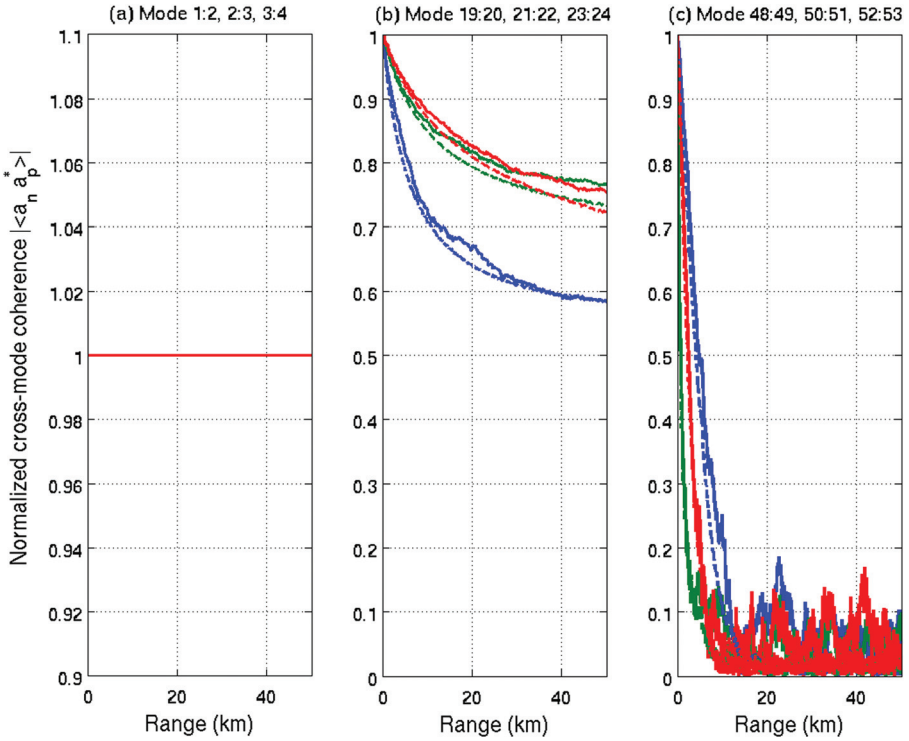

FIG. 6. Normalized mode coherences for the case with surface waves alone. Shown are coherences for mode pairs: (a) 1 with 2 (blue), 2 with 3 (green), and 3 with 4 (red), (b) 19 with 20 (blue), 21 with 22 (green), and 23 with 24 (red), and (c) 48 with 49 (blue), 50 with 51 (green), and 52 with 53 (red). Monte Carlo simulations are shown as the solid line, and transport theory the dashed line.

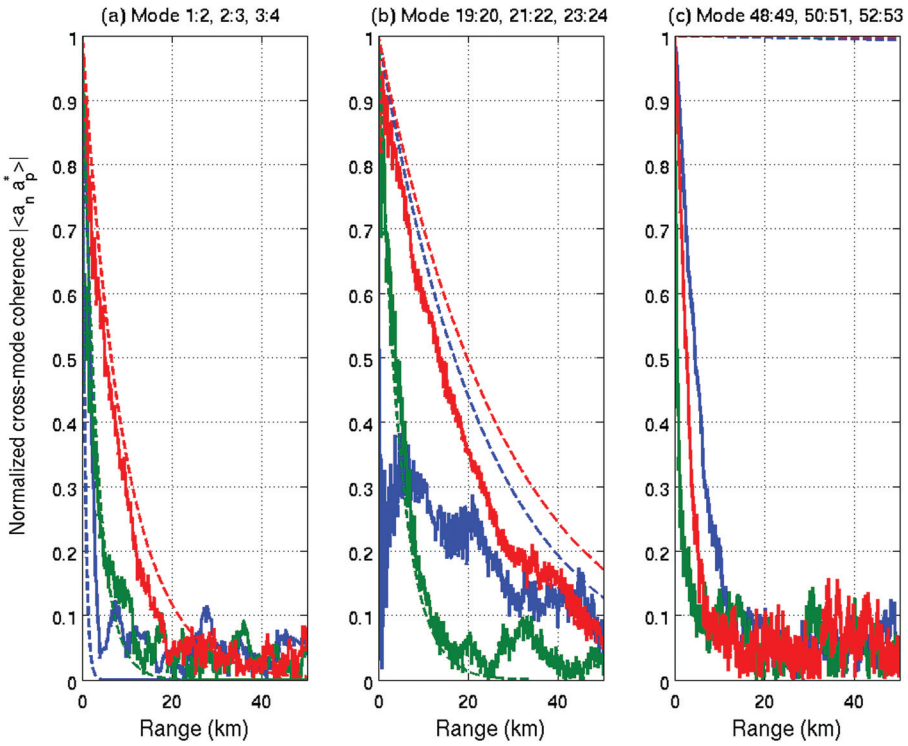

FIG. 7. Normalized mode coherences for the case with surface and internal waves. Shown are coherences for mode pairs: (a) 1 with 2 (blue), 2 with 3 (green), and 3 with 4 (red), (b) 19 with 20 (blue), 21 with 22 (green), and 23 with 24 (red), and (c) 48 with 49 (blue), 50 with 51 (green), and 52 with 53 (red). Monte Carlo simulations are shown as the solid line, and hybrid transport theory the dashed line. Also of note are that mode coherences as predicted by the hybrid transport theory in (c) are equal to 1.

D. Mode coherences

The effect of surface waves in the absence and presence of internal waves on the cross-mode coherence is now presented and compared to Monte Carlo simulations.

Figure 6 shows the range evolution of normalized mode coherences [i.e., $|\langle a_n a_p^* \rangle|(r)/\sqrt{\langle |a_n|^2 \rangle(r)\langle |a_p|^2 \rangle(r)}$] for three sets of low (mode 1 with 2, 2 with 3, 3 with 4), medium (mode 19 with 20, 21 with 22, 23 with 24), and high modes (mode 48 with 49, 50 with 51, 52 with 53), for the case with surface waves alone, for a wind speed of 5.5 m/s. Figure 7 shows mode coherences when both surface and internal waves are present. Transport theory results shown by the dashed line and Monte Carlo simulations are shown by the solid line.

The cross-mode coherence for surface waves is calculated using the full-coherence equation, Eq. (6), for a wind speed of 5.5 m/s. The range evolution of mode coherences computed using Monte Carlo simulations are shown to be in good agreement with transport theory results. In Fig. 6, uncoupled lower modes are seen to be perfectly coherent, and the rate of coherence loss increases with mode number, consistent with the increasing strength of mode coupling. Thus, unlike the case with internal waves (Colosi *et al.*, 2012a; Raghukumar and Colosi, 2014) where the loss of coherence was well-modeled by adiabatic transport theory, surface wave-induced loss of coherence is an effect of mode coupling. The inclusion of internal waves in the perturbation scenario (Fig. 7) results in numerical artifacts in the coherence calculation, which partly motivated the hybrid transport theory approach proposed by Raghukumar and Colosi (2014). In this hybrid approach, the cross-mode coherence was given as

$$\langle a_n a_p^* \rangle(r) = \langle |a_n|^2 \rangle^{1/2}(r)\langle |a_p|^2 \rangle^{1/2}(r) e^{i(\theta_n(0)+\theta_p(0))} \times e^{i(k_n-k_p)r} e^{-(I_{nn,nn}-2I_{nn,pp}+I_{pp,pp})r}, \quad (21)$$

where θ_n is the initial phase of the mode n (for a point source, θ_n is either 0 or π), and $I_{mn,qp}$ is the internal wave scattering matrix [Eq. (13)] in the adiabatic approximation ($k_{qp} = 0$). Here, $\langle |a_n|^2 \rangle^{1/2}(r)$ are the range dependent mode amplitudes caused by mode coupling. While this approach models low internal wave-coupled mode coherences adequately, the adiabatic approximation is clearly incorrect for the higher surface wave-coupled modes. However, we argue that this approach serves to clearly demonstrate the importance of including acoustic mode coupling by surface waves in coherence calculations.

It can be reasonably concluded that in the presence of both internal and surface waves, loss of coherence occurs by two mechanisms: (1) the random advance and delay of lower order modes with turning depths in the thermocline, where sound speed perturbations by internal waves are the largest, and (2) mode coupling of higher order modes, with turning depths at or near the surface.

E. Mean intensity

Having examined individual components of the cross-mode coherence matrix, such as mode energies and mode coherence, under two perturbation scenarios with a focus on mode coupling in the absence of attenuation, the acoustic observable of mean intensity is now presented, in the

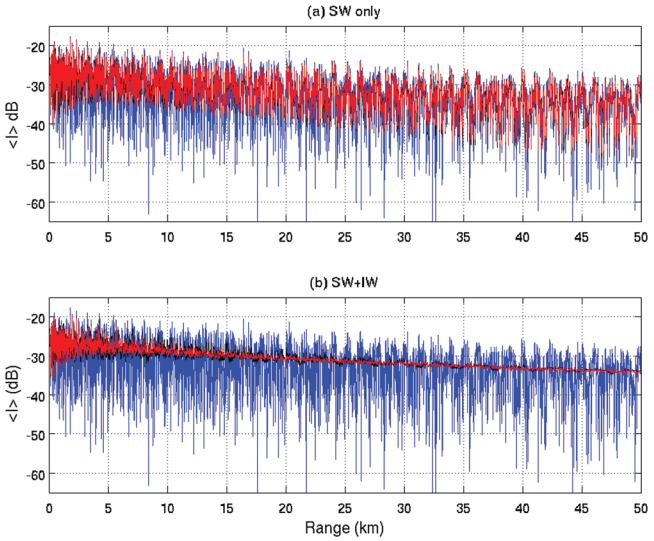

FIG. 8. Mean intensity (dB) for a receiver at a depth of 50 m, for the unperturbed environment (blue line), transport theory (black line), and Monte Carlo simulation (red line). Shown are mean intensities with (a) surface waves alone and (b) surface and internal waves.

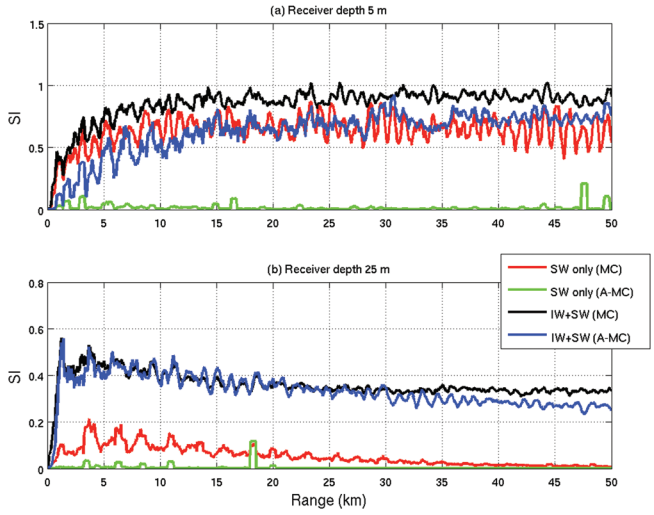

FIG. 9. Range evolution of the SI for a receiver at (a) 5 m and (b) 25 m. Shown are the Monte Carlo and adiabatic Monte Carlo simulations for the case with surface waves alone (red and green lines, respectively), and surface and internal waves (black and blue lines, respectively).

presence of mode attenuation. Figure 8 shows the mean intensity in decibels, calculated using Eq. (5), for a receiver located at a depth of 50 m, in the presence of surface waves (upper panel), and surface and internal waves (lower panel). Shown are the unperturbed intensity (blue line), Monte Carlo simulation (red line), and transport theory (black line).

Mean intensities for surface waves alone, Fig. 8(a), are calculated using the full coherence approach with the cross-mode coherence matrix given by Eq. (6). The transport theory results show excellent agreement Monte Carlo simulations. The preferential coupling and phase randomization of rapidly attenuating high modes by surface waves is seen to result in the mean intensity increasingly resembling the unperturbed intensity due to the eventual dominance of uncoupled low modes on the mean intensity.

Mean intensities when both internal and surface waves are present, Fig. 8(b), are calculated using the hybrid approach for mode coherences, as presented in Raghukumar and Colosi (2014). Interestingly, despite the limitations of that approach in modeling high mode coherences, the mean intensity as calculated still shows excellent agreement with Monte Carlo simulations. This is easily explained by the fact that high modes, whose coherences are incorrectly calculated using the hybrid approach, experience rapid attenuation, and contribute significantly less to the mean intensity than the correctly modeled low mode coherences. As a result, the mean intensity in the presence of both internal and surface waves, under the studied perturbation scenario, closely resembles that with internal waves alone (Raghukumar and Colosi, 2014). This is, however, not necessarily the case at higher wind speeds, where there is the potential for additional contribution to the mean intensity from a larger number of medium to high modes.

F. Scintillation Index (SI)

The SI is a useful measure of the intensity variance, and can be expressed in terms of the intensity, I, as

$$\mathrm{SI} = \langle I^2 \rangle / \langle I \rangle^2 - 1. \tag{22}$$

Figure 9 shows Monte Carlo simulations of the range evolution of the SI for two receivers at 5 and 25 m depths, for the cases with surface waves, and surface and internal waves. Also shown are the adiabatic Monte Carlo simulations that ignore mode coupling and the off-diagonal terms of the cross-mode coherence matrix. A moving average filter over 500 m is applied to all curves for clarity. Transport theory calculations for the SI (not shown), using the hybrid and adiabatic transport theories, were seen to be similar to the adiabatic Monte Carlo simulations.

For the case with surface waves alone, the importance of mode coupling phenomena in acoustic propagation is reiterated in the SI. This is particularly evident for the shallow receiver where only surface wave-coupled high modes dominate the coupling regime. The SI asymptotes close to 0.8 (red curve), and the absence of any SI excursions above 1 indicates a diffractive acoustic scattering regime that is in between an unsaturated field and a fully saturated field (Colosi and Baggeroer, 2004). The adiabatic calculation (green curve) that ignores mode coupling is significantly lower. The discrepancy with adiabatic theory persists at smaller ranges at the deeper depth, but at a considerably smaller SI. This is largely due to the contribution to intensity fluctuations from high modes which oscillate throughout the water column unlike the low modes which are evanescent away from the thermocline, and do not contribute to intensity fluctuations from surface waves. At a depth of 25 m, the SI asymptotes close to zero, indicating an unsaturated acoustic field at depth.

The addition of internal waves to the scattering scenario, and the resulting phase randomization of all modes across the mode spectrum drives the SI to saturation at the shallow receiver (black curve). The contribution to the SI calculated using the adiabatic approximation, from internal wave scattered modes is significant (blue curve), even at this shallow

receiver. This contribution is largely from modes 18–21 that have turning depths above 10 m [see Fig. 5, Raghukumar and Colosi (2014)], but continue to experience internal wave effects (Fig. 3). Moving the receiver closer to the surface (not shown) has the effect of reducing contributions from internal waves to the adiabatic SI (lowering of the blue curve), and further saturating the SI due to even greater surface wave contributions (rising of the red curve). At depth, the dominance of phase randomization by sound speed perturbations from internal waves results in a close agreement of the adiabatic simulation with the full-field calculation, in addition to a significantly higher SI that asymptotes close to 0.3.

V. DISCUSSION AND CONCLUSION

An efficient reduced-physics transport theory for surface wave scattering, previously proposed by Thorsos *et al.* (2010), was merged with that for random linear internal wave scattering in shallow water (Colosi *et al.*, 2012b), extended to a high-frequency regime by Raghukumar and Colosi (2014). As before, the propagation environment was chosen to mimic conditions encountered during the SW06 experiment off the New Jersey coast. Modeled surface and internal wave parameters such as the wind speed and internal wave energy spectra were realistically chosen based on known measurements during the SW06 (Colosi *et al.*, 2012a; Dahl, 2010). A numerically tractable form for the surface wave scattering matrix was proposed when the sea surface is modeled by the PM isotropic spectrum. Transport theory results were then validated against Monte Carlo simulations, and important insights into mode coupling phenomena were presented.

Surface waves were shown to preferentially couple high modes with turning depths at the surface, a contrast to internal waves that preferentially couple low modes with turning depths in the thermocline, the region of strongest internal wave activity. Using this rather intuitive result, it was then shown that the presence of both surface and internal waves causes mode coupling across the entire mode spectrum, with important consequences to acoustic observables such as the mean and variance of intensity. Previously proposed metrics such as the competition between the mode coupling range versus the attenuation range were applied to acoustic propagation with surface waves. Unlike internal wave scattering, where low modes had coupling ranges shorter than attenuation ranges, surface wave scattering causes high modes to have coupling ranges shorter than attenuation ranges. This allows the high modes to couple and exchange mode energies before they are attenuated by the water column and seabottom. While increased wind speeds result in the shortening of mode coupling ranges, they do not necessarily imply that a larger number of high modes are coupled. The presence of a mode cutoff determined by the mode turning depth prevents mode numbers below this cutoff from being coupled by surface waves, regardless of wind speed. Similarly, it was shown that while the strength of mode coupling increases with increasing wind speed, the mode-number cutoff, below which lower modes can be coupled by surface waves, is relatively unaffected.

The preferential coupling of high modes by surface waves was reiterated in the range evolution of mean mode energies, which were shown to be in good agreement with Monte Carlo simulations. The presence of both internal and surface waves was then shown to result in the approach to equipartition of all modes across the mode spectrum. Surface waves also caused the preferential loss of cross mode coherences for the high modes. In the presence of both internal and surface waves, while numerical artifacts prevented an accurate transport-theoretic evaluation of the cross-mode coherence matrix, the hybrid approach proposed by Raghukumar and Colosi (2014) was shown to sufficiently reproduce the acoustic observable of mean intensity. The hybrid approach, which ignores mode coupling effects on mode coherences in the presence of internal waves (adiabatic approximation), incorrectly models high mode coherences of surface wave-coupled modes. Despite this deficiency, the attenuation of high modes with increasing range minimizes their contribution to mean intensity, resulting in the accurate modeling of mean intensity by the hybrid approach. The Monte Carlo simulations of mode coherence clearly illustrate the loss of mode coherence across the entire mode spectrum, resulting in an observed mean intensity pattern that is devoid of any interference pattern.

Finally, second-moment statistics of intensity were demonstrated via Monte Carlo simulations of the SI for a receiver at two different depths. For a receiver close to the surface, the dominance of mode coupling effects by surface waves resulted in a SI much higher than that modeled using the adiabatic approximation. The addition of internal waves to the propagation scenario results in a SI that is dominated by roughly four medium-order modes with shallow turning depths. Consequently the SI is now somewhat better modeled using the adiabatic approximation. The inclusion of surface and internal wave mode coupling phase terms to the calculation results in a SI indicative of a fully-saturated acoustic field, consistent with the loss of coherence across the entire mode spectrum. At depth, it was then shown that the adiabatic approximation sufficiently models the SI when internal waves are the dominant perturbation phenomenon.

These results point to an interesting phenomena where in the presence of both internal and surface waves, there are two co-existing mode coupling regimes, the first being the low mode coupling by internal waves and the loss of coherence across roughly the first half of the mode spectrum, well-modeled by the adiabatic transport theory. The second regime is the mode coupling of high modes, and the loss of mode coherence by mode coupling for the second half of the mode spectrum, which requires the use of a full-coupled transport theory. The separation of these two regimes occurs at mode numbers where the upper turning depth leaves the thermocline and encounters the surface.

Some limitations of the current study include the assumption of range-independence and anisotropy of surface and internal wave spectra. One might reasonably expect the spectra to vary over a 50 km range, particularly in a shallow water environment. However, it should be pointed out that there is no theoretical requirement of range-independence in the transport theory presented, and range-dependence is

simply a matter of implementation of a range-dependent scattering matrix. This is easily accomplished by the inclusion of a range-dependent energy parameter for internal waves, and a range-dependent wind speed for surface waves. Regarding anisotropy, a preliminary analysis of SW06 mooring data indicates that stochastic internal waves have a cross-shore energy that is almost twice the alongshore energy. The surface wave spectrum is also modeled as being isotropic, an approximation that from the point of view of acoustic mode transport, only applies to weak scattering measured isotropically. The treatment of anisotropy to handle stronger acoustic scattering is beyond the scope of the transport theory in its current form. One might also question the applicability of a PM spectrum for fully-developed seas in this study where transport theory calculations were made for a low wind speed of 5.5 m/s. We argue that this low wind speed was chosen based on wind measurements during SW06, and the limitation on wind speeds in the surface wave transport theory (Thorsos *et al*., 2010) that allows the surface wave mode coupling matrix to only vary linearly with sea surface height perturbations. Further, while this paper utilized the PM spectrum for surface waves, any spectral form will suffice for the transport theory.

ACKNOWLEDGMENTS

This work was supported by the Office of Naval Research. K.R. is grateful to the National Academy of Sciences for support through the National Research Council research associateship program. The authors thank Frank Henyey at the Applied Physics Laboratory, University of Washington, for several useful discussions and his assistance with the Monte Carlo simulations.

[1]The $\mathrm{sgn}(k_{pq})$ term in Eq. (9) is missing in Colosi *et al*. (2012a), Eq. (11). The $\mathrm{sgn}(k_{pq})$ term is also missing in Raghukumar and Colosi (2014), Eqs. (A2) and (11).

Beilis, A., and Tappert, F. D. (**1979**). "Coupled mode analysis of multiple rough surface scattering," J. Acoust. Soc. Am. **66**, 811–826.

Brown, M. V. (**1969**). "Intensity fluctuations in reflections from the ocean surface," J. Acoust. Soc. Am. **46**, 196–204.

Colosi, J. A., and Baggeroer, A. B. (**2004**). "On the kinematics of broadband multipath scintillation and the approach to saturation," J. Acoust. Soc. Am. **116**, 3515–3522.

Colosi, J. A., and Brown, M. G. (**1998**). "Efficient numerical simulations of stochastic internal wave induced sound speed perturbation fields," J. Acoust. Soc. Am. **103**, 2232–2235.

Colosi, J. A., Chandrayadula, T., Voronovich, A., and Ostashev, V. (**2013**). "Coupled mode transport theory for sound transmission through an ocean with random sound speed perturbations: Coherence in deep water environments," J. Acoust. Soc. Am. **134**, 3119–3133.

Colosi, J. A., Duda, T. F., Lin, Y.-T., Lynch, J. F., Newhall, A. E., and Cornuelle, B. D. (**2012a**). "Observations of sound-speed fluctuations on the New Jersey continental shelf in the summer of 2006," J. Acoust. Soc. Am. **131**, 1733–1748.

Colosi, J. A., Duda, T. F., and Morozov, A. K. (**2012b**). "Statistics of low-frequency normal-mode amplitudes in an ocean with random sound-speed perturbations: First and second moments of intensity in shallow-water environments," J. Acoust. Soc. Am. **131**, 1749–1761.

Colosi, J. A., and Morozov, A. K. (**2009**). "Statistics of normal-mode amplitudes in an ocean with random sound-speed perturbations: Cross coherence and mean intensity," J. Acoust. Soc. Am. **126**, 1026–1035.

Creamer, D. B. (**1996**). "Scintillating shallow water waveguides," J. Acoust. Soc. Am. **99**, 2825–2838.

Dahl, P. H. (**1999**). "On bistatic sea surface scattering: Field measurements and modeling," J. Acoust. Soc. Am. **105**, 2155–2169.

Dahl, P. H. (**2010**). "Observations and modeling of angular compression and vertical spatial coherence in sea surface forward scattering," J. Acoust. Soc. Am. **127**, 96–103.

Dozier, L. B. (**1982**). "A coupled-mode model for spatial coherence of bottom-interacting energy," in *Proceedings of the Stochastic Modeling Workshop*, edited by C. W. Spofford and J. M. Haynes (ARL-University of Texas, Austin, TX), pp. 28-1–28-46.

Dozier, L. B., and Tappert, F. D. (**1978a**). "Statistics of normal mode amplitudes in a random ocean. I. Theory," J. Acoust. Soc. Am. **63**, 353–365.

Dozier, L. B., and Tappert, F. D. (**1978b**). "Statistics of normal mode amplitudes in a random ocean. II. Computations," J. Acoust. Soc. Am. **64**, 533–547.

Eckart, C. (**1953**). "The scattering of sound from the sea surface," J. Acoust. Soc. Am. **25**, 566–570.

Garrett, C., and Munk, W. H. (**1979**). "Internal waves in the ocean," Ann. Rev. Fluid Mech. **11**, 339–369.

Henyey, F. S., and Thorsos, E. I. (**2013**). "Propagation effects of surface waves in two unperturbed mode models," J. Acoust. Soc. Am. **134**, 4113–4113.

Jensen, F. B., Kuperman, W. A., Porter, M. B., and Schmidt, H. (**1994**). *Computational Ocean Acoustics* (AIP, Woodbury, NY), Chap. 5.8.

Lynch, J. F., and Tang, D. (**2008**). "Overview of shallow water 2006 JASA EL Special Issue Papers," J. Acoust. Soc. Am. **124**, EL63–EL65.

McDaniel, S. T. (**1993**). "Sea surface reverberation: A review," J. Acoust. Soc. Am. **94**, 1905–1922.

Munk, W. H., Worcester, P. F., and Wunsch, C. (**1995**). *Ocean Acoustic Tomography* (Cambridge University Press, Cambridge), Chap. 5.

Olbers, D. J., and Herterich, K. (**1979**). "The spectral energy transfer from surface waves to internal waves," J. Fluid Mech. **92**, 349–379.

Pierson, M., and Moskowitz, L. (**1964**). "A proposed spectral form for fully developed wind seas based on the similarity theory of S. A. Kitaigorodskii," J. Geophys. Res. **69**(24), 5181–5190, doi: 10.1029/JZ069i024p05181.

Raghukumar, K., and Colosi, J. A. (**2014**). "High frequency normal mode statistics in a shallow water waveguide: The effect of random linear internal waves," J. Acoust. Soc. Am. **136**, 66–79.

Rouseff, D., and Ewart, T. E. (**1995**). "Effect of random sea surface and bottom roughness on propagation in shallow water," J. Acoust. Soc. Am. **98**, 3397–3404.

Tang, D., Moum, J. N., Lynch, J. F., Abbot, P., Chapman, R., Dahl, P. H., Duda, T. F., Gawarkiewicz, G., Glen, S., Goff, J. A., Graber, H., Kemp, J., Maffei, A., Nash, J. D., and Newhall, A. E. (**2007**). "Shallow water' 06—A joint acoustic propagation/Nonlinear internal wave physics experiment," Oceanogr. **20**, 156–167.

Thorsos, E. I. (**1988**). "The validity of the Kirchhoff approximation for rough surface scattering using a Gaussian roughness spectrum," J. Acoust. Soc. Am. **83**, 78–92.

Thorsos, E. I. (**1990**). "Acoustic scattering from a 'Pierson-Moskowitz' sea surface," J. Acoust. Soc. Am. **88**, 335–349.

Thorsos, E. I., Henyey, F. S., Elam, W. T., Hefner, B. T., Reynolds, S. A., and Yang, J. (**2010**). "Transport theory for shallow water propagation with rough boundaries," AIP Conf. Proc. **1272**, 99–105.

Thorsos, E. I., Henyey, F. S., Elam, W. T., Reynolds, S. A., and Williams, K. L. (**2004**). "Modeling shallow water propagation with scattering from rough boundaries," AIP Conf. Proc. **728**, 132–140.

Watson, K. M. (**1994**). "Energy transfer between surface and internal waves in the North Pacific Ocean," J. Geophys. Res. **99**, 12549–12560, doi:10.1029/94JC00570.